Spatial Orientation of Galaxies in the Substructures of SDSS Supercluster S[184+003+0077]

Janak Ratna Malla[1], Walter Saurer[2], Binil Aryal[3]
[1] Central Department of Physics, Tribhuvan University, Kirtipur, Nepal
[2] Institute of Astroparticle Physics, Innsbruck University, Innsbruck, Austria
[3] Institute of Science & Technology, Tribhuvan University, Kirtipur, Nepal
binil.aryal@cdp.tu.edu.np
(Submitted on 18.10.2021. Accepted on 22.02.2022)

Abstract. We present substructures and preferred alignments of 1 365 galaxies in the supercluster S[184+003+0077]. A study of the magnitude, color, redshift and number density of the nearest neighbor galaxies was carried out. The 'galaxy counting code' is used to count nearest neighbors of each galaxy by varying the radius. We found 4 substructures in the supercluster region. An empirical relation between the number of galaxies and mean redshift of substructures is observed. The spatial distribution of the angular momentum vectors of galaxies in the supercluster and its substructures are studied. The selection effects in the database are removed using the random simulation method. The observed distributions of the angular momentum vectors of galaxies are compared with the expected theoretical distribution using chi-square, auto-correlation and Fourier tests. No preferred alignments of the angular momentum vectors of galaxies are noticed in the supercluster S[184+003+0077], supporting the hierarchy model. In the substructures, local groupings are observed.
Key words: Galaxies: evolution galaxies: superclusters galaxies: statistics

1 Introduction

Superclusters are the largest observed structures in the Universe. A supercluster constitutes several clusters and groups of galaxies which are a gravitationally bound system. A large database of superclusters is available in the Sloan Digital Sky Survey Data Release 7 (SDSS DR7 hereafter) and the pioneer work by Einasto et al. (2003, 2011, 2014, 2016). Einasto et al. (2003) investigated superclusters of galaxies in the SDSS and found that the clusters located at high-density environment showed luminosity a factor of 5-10 times higher than in low-density environment of the field. Further Einasto et al. (2011) classified the morphology of a set of superclusters using the SDSS DR7 database and calculated their luminosity to determine superclusters from a flux-limited sample of galaxies and finally selected superclusters with 300 and more galaxies. A widely different morphology of superclusters is found. In the next paper, Einasto et al. (2014) compared the galaxy populations in SDSS superclusters of different morphology in the nearby Universe ($180\ h^{-1}$Mpc $< d < 270\ h^{-1}$Mpc) and concluded that both the local (group) and global (supercluster) environments play an important role in the formation and evolution of galaxies. In the same year, Einasto et al. (2016) studied the dynamical state of galaxy superclusters from the Sloan Great Wall (SGW) which is the richest galaxy system in the nearby Universe. They concluded that the rich SGW superclusters with their high-density cores represent dynamically evolving environments, which are well suited for studies of the properties of galaxies and galaxy systems.

Von Weizsäcker and Gamow (1951 & 1952) predicted that the angular momentum of galaxies can explore the initial conditions under which these systems formed. The distribution of the angular momentum of galaxies in the

supercluster might reveal the origin of the early universe. There have been a handful of studies in the past, predicting three galaxy formation scenarios: the 'pancake model' (Shandarin 1974) predicts that the rotation axes (i.e., angular momentum vectors) of galaxies tend to lie within the cluster plane whereas the 'primordial vorticity model' (Ozernoy 1978) claims that the rotation axes of galaxies tend to be oriented perpendicular the cluster plane. The 'hierarchy model' (Peebles 1969) predicts a random orientation.

In order to understand the formation and evolution of a supercluster, its substructures and their spatial orientation should be well understood. In the present work, we aim to study as follows: (a) the color-magnitude diagram, (b) the number density maps, (c) identify individual substructures in the supertructures, (d) study the preferred alignments of angular momentum vectors of galaxies in the substructures in the superclusters, and finally (e) compare subclustering and the preferred alignments with the galaxy evolution models.

2 SDSS Supercluster S[184+003+0077]

We have compiled a database (positions, redshifts, r- and u-magnitudes) of 1 365 galaxies in the supercluster S[184+003+0077] using the SDSS database. The all sky distribution of galaxies in the superclusters is shown in Fig. 1a. A marker galaxy in the supercluster is the brightest galaxy near the highest density peak in the supercluster volume (Liivamägi et al., 2012). The aim of this is to tie a supercluster to an already observed cross identifier.

Fig. 1b shows the redshift contour map of the supercluster region. Redshift is found to be distributed in such a way that the marker galaxy lies in the low redshift region, whereas it is surrounded by a high redshift region. We have analyzed the magnitude (m_r), color (m_u-m_r) and redshift (z) distributions of galaxies in the supercluster. The color ($\log(m_u$-$m_r)$) – magnitude (m_r) diagram (Fig. 1c) is fitted by

$$\log(m_u - m_r) = -0.04 m_r + 1.08 \tag{1}$$

Here the slope is found to be slightly negative, suggesting that the color is mostly independent of magnitude.

3 Methods

We have determined the number density around each galaxy using an algorithm named 'galaxy counting code' (Appendix A). The variable is the radius (r) from each and every galaxy. We set the values of r from 0.1° to 2.0° in steps of 0.05°. We determined the standard deviation in each step. Then selected the steps where the standard error of the deviation is found to be maximum. In addition, the least number of galaxies in the substructures has been set as the cutoff values of that particular standard deviation.

We have used the method developed by Flin & Godlowski (1986) to find the angular momentum vectors of a galaxy. In their method, the angular momentum vector is defined by two angles: polar (θ) and azimuthal (ϕ):

$$\begin{aligned} \sin\theta &= -\cos i \sin\delta \pm \sin i \sin P \cos\delta \\ \sin\phi &= (\cos\theta)^{-1}[-\cos i \cos\delta \sin\alpha + \sin i \\ &\quad (\mp \sin P \sin\delta \sin\alpha \mp \cos P \cos\alpha)] \end{aligned} \tag{2}$$

where α, δ, P and i are the right ascension (R.A.), declination (Dec.), equatorial position angle, and the inclination angle, respectively. The inclination angle (i) of galaxies is calculated using Holmberg's (1946) formula: $\cos^2 i = [(b/a)^2 – q^2]/(1–q^2)$ with b/a the measured axial ratio (b/a) and q the intrinsic flatness. We run a numerical simulation to find the expected isotropic distribution (Aryal & Saurer 2000). Our observations are compared with isotropic distribution curves in both θ and ϕ. For this we use three statistical tests: chi-square, Fourier, and auto correlation, as suggested by Aryal et al. (2007).

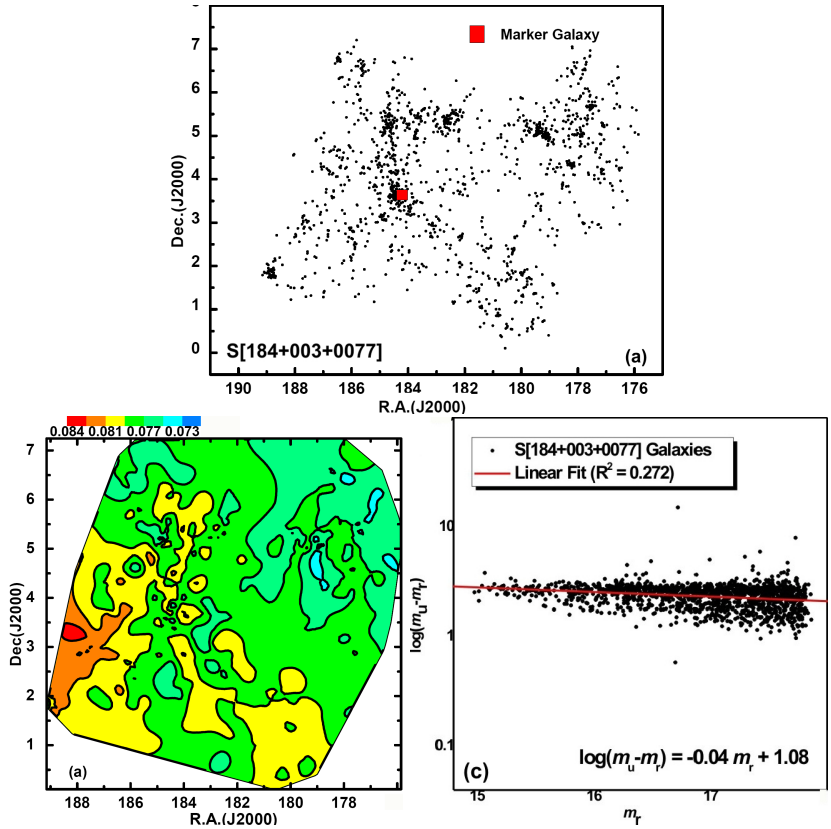

Fig. 1. (a) Sky distribution of the galaxies in the supercluster S[184+003+0077]. Each open circle represents a galaxy. The marker galaxy is denoted by a filled square. (b) The redshift map of the supercluster region. The redshift color bar is shown as well. (c) Color ($\log(m_u$-$m_r)$-magnitude (m_r) diagram of galaxies in the supercluster S[184+003+0077]. Each black dots represents a galaxy. The best fit lines and equation are shown.

For the plotting and statistics, we use the software ORIGIN 8.0. To count the nearest neighbor galaxies within a radius r, a code was written using MATLAB 6.1.

4 Results & Discussion

Fig. 2a,b shows the number density map of the galaxies in the supercluster S[184+003+0077]. The contour levels and the color bars are shown. We consider the region of high density as a substructure of the supercluster. In the supercluster S[184+003+0077], we noticed 4 such regions in which the number density of galaxies exceeds the limits of the standard deviation. The respective number of galaxies in these substructures is found as 170, 91, 68 and 70. The names of substructures are given as S1[185+0035+0077], S2[180+0050+0079], S3[185+0050+0079] and S4[183+0050+0080]. The mean values of the magnitude (m_r) of these substructures are listed in the third column of Table 1.

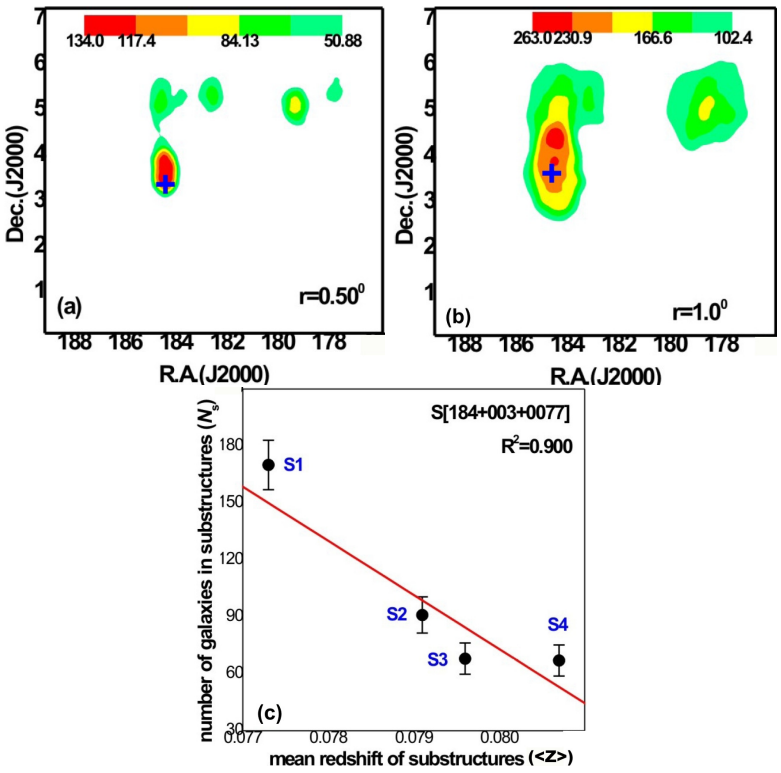

Fig. 2. Number density map of galaxies in the supercluster S[184+003+0077]. Nearest neighbor distance of each galaxies at $r = 0.5^\circ$ (a) and 1.0° (b). The color bars are shown. (c) Number of galaxies in substructures versus mean redshift plot in the supercluster S[184+003+0077]. The statistical $\pm 1\sigma$ error bars are shown. Here S1, S2, S3, S4 represent substructures in the supercluster. The coefficient of regression is shown.

Fig. 2c shows a plot of the number of galaxies in the substructures versus the mean redshift ($< z >$) of that substructure.

The best fit line is,

$$N = -2.8 \times 10^4 < z > +2353.2 \quad (3)$$

Substructures S2 and S3 showed similar values of the mean redshift ($< z >$) and magnitude (m_r) (Fig. 2a,c & Table 1), suggesting a close association between them. They are either in the process of aggregation or separation. Therefore, the angular momentum vectors of these two groups are expected to show peculiarities.

We study the spatial orientation of the angular momentum vectors of galaxies with respect to the equatorial coordinate system. Any deviation from the expected isotropic distribution will be tested using four statistical parameters, namely the chi-square probability (P$> \chi^2$), auto-correlation coefficient (C/C(σ)), first order Fourier coefficient $\Delta_{11}\sigma(\Delta_{11})$, and first order Fourier probability (P$> \Delta_1$). The conditions for anisotropy are the following: P($> \chi^2$) < 0.050, C/C(σ) and $\Delta_{11}/\sigma(\Delta_{11}) > 1$, and P($> \Delta_1$) < 0.150. These statistical limits were proposed by Godlowski (1994). The polar (θ) and azimuthal (ϕ) angle distributions of galaxies in S[184+003+0077] are shown in Fig. 3. The statistical values are listed in Table 1. In the supercluster S[184+003+0077], the value of the chi-square probability [P($>\chi^2$)] is found to be 0.084, suggesting no preferred alignments. A similar trend is shown by the auto-correlation test [C/C(σ)=1.0]. The first order Fourier coefficient [$\Delta_{11}/\sigma(\Delta_{11})$] and Fourier probability [P($>\Delta_1$)] are found to be 0.6 and 0.790, suggesting isotropy.

A very good agreement between the observed (solid circle with error bars) and expected (solid line) distributions can be seen in Fig. 3a. At $\theta = 27.5°$, a hump can be seen. There is a larger number of observed galaxies (285) than the expected (250). Thirty five galaxies showed a preferred alignment at this angle. This preference might be because of a sub-clustering phenomena due to the tidal or gravitational shearing effect. In the azimuthal angle distribution (Fig. 3b), the observed and expected distributions are in closer agreement. All four statistical parameters [(P($>\chi^2$), C/C(σ), $\Delta_{11}/\sigma(\Delta_{11})$] and P($>\Delta_1$) suggest isotropy (Table 1). This means that, the projections of the angular momentum vectors of galaxies in S[184+003+0077] showed no preference. In the shaded region, at $\phi = -5°$, a hump can be seen at the 2σ level. But this hump is cancelled by two dips at $-45°$ and $5°$. Therefore, vanishing angular momentum is noticed in the supercluster.

The polar and azimuthal angle distributions of galaxies in four substructures of the supercluster S[184+003+0077] are shown in Fig. 4. The largest substructure S1[185+0035+0077] consists of 170 galaxies. This means that, redshift ($< z >$) is similar to that of the supercluster. In the polar angle (θ hereafter) distribution, the value of the chi-square probability [P($> \chi^2$)] and first order Fourier probability [P($> \Delta_1$)] are found to be 0.648 and 0.623. Both these probabilities are more than 60%, suggesting no preferred alignments. Similarly, the auto-correlation [C/C(σ)] and first order Fourier coefficients [$\Delta_{11}/\sigma(\Delta_{11})$] are found to be less than one, suggesting isotropic distribution. In the azimuthal angle (ϕ hereafter) distribution of substructure S1, three statistical parameters namely P($> \chi^2$), P($> \Delta_1$) and $\Delta_{11}/\sigma(\Delta_{11})$ showed isotropy (Table 1). Only the auto correlation coefficient [C/C(σ)] showed a

Table 1. Statistics of the polar (θ) and azimuthal angle (ϕ) distributions of galaxies in the supercluster S[184+003+0077] and its four substructures S1[185+0035+0077], S2[180+0050+0079], S3[185+0050+0079] and S4[183+0050+0080]. The first column lists the name of the supercluster and its substructures. The second and third columns give R.A.(J2000), number of galaxies (N), Dec.(J2000) and mean values of (m_r) magnitude. The fourth and fifth columns list the values of the chi-square probability (P($> \chi^2$)) and auto-correlation coefficient [C/C(σ)]. The last two columns give the first order Fourier coefficient [$\Delta_{11}/\sigma(\Delta_{11})$] and the first order Fourier probability [P($> \Delta_1$))], respectively.

subsample			P($>\chi^2$)	C/C(σ)	$\Delta_{11}/\sigma(\Delta_{11})$	P($>\Delta_1$)
polar angle	RA(J2000)	N				
S[184+003+0077]	183.815°	1365	0.084	+1.0	+0.6	0.790
S1[185+0035+0077]	179.205°	170	0.648	+0.9	+0.9	0.623
S2[180+0050+0079]	182.579°	91	0.888	+0.2	−0.2	0.973
S3[185+0050+0079]	184.378°	68	0.912	+0.1	+0.3	0.904
S4[183+0050+0080]	177.450°	67	0.815	−0.4	-0.5	0.846
azimuthal angle	Dec.(J2000)	m_r				
S[184+003+0077]	+3.358°	17.9	0.580	+0.3	+0.8	0.490
S1[185+0035+0077]	+3.601°	17.8	0.129	−1.1	+0.5	0.860
S2[180+0050+0079]	+5.038°	17.9	0.960	−0.1	−0.3	0.909
S3[185+0050+0079]	+5.350°	17.8	0.339	−1.1	−0.7	0.712
S4[183+0050+0080]	+5.639°	18.0	0.822	−0.1	+0.5	0.885

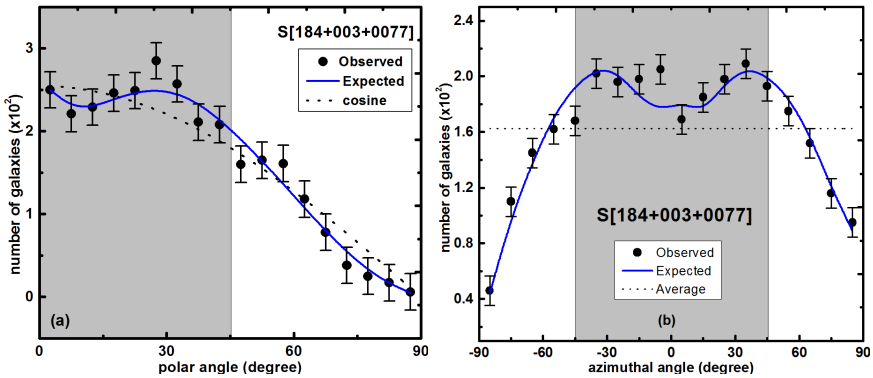

Fig. 3. Polar (a) and azimuthal angle (b) distributions of galaxies in the supercluster S[184+003+0077]. The solid curves represent the expected distributions. The dotted curves show the cosines (a) and average (b) distributions. The statistical $\pm 1\sigma$ error bars are shown.

weak deviation (1.1σ) from isotropy. In Fig. 4a, a number of humps (12.5°, 27.5°, 32.5°) and dips (2.5°, 42.5°) at small angles suggest a local effect, supporting the formation of subgroups within the substructure S1. These effects are possibly enhanced by the tidal effect, due to which the angular momentum vectors of neighboring galaxies get affected (Godlowski, 2012). However, these humps and dips cancel each other to show isotropy. Four alternative humps (−25°, −5°, 15°, 45°) and dips (−45°, −15°, 5°, 35°) can be seen in the ϕ distribution (Fig. 4b). A hump followed by a dip suggests either a binning effect in the histogram or a successive deviation of the angular momentum vectors and their projections due to subclustering. In the substructure S2, there are 91 galaxies with mean redshift ($< z >$) 0.079 which is slightly larger than that of the supercluster as a whole. Therefore, substructure S2 is moving away with a relatively larger speed than that of substructure S1. Thus, the effect of gravitational shearing can not be denied here. Let us discuss its effect in the alignments. The distributions of the angular momentum vectors (polar angle, θ) and their projections (azimuthal angle, ϕ) of galaxies in the substructures S2 are shown in Figs. 4c,d. All eight statistical values in both θ and ϕ distributions suggest isotropy (Table 1). Similar to the substructure S1, this substructure showed several systematic humps and dips in both the θ and ϕ distributions. Instead of alternate humps and dips, here we noticed successive groups of deviations (for example, 12.5° to 32.5°, 37.5° to 57.5° in Fig. 4c and −75 to −55°, −15 to 5° in Fig. 4d) from the expected. In the statistical tests, these deviations cancel each other to show isotropy in both the θ and ϕ distributions.

Substructure S3 has exactly the same values of the mean redshift as S2. This means that, both substructures are moving with identical radial velocities. Fig. 4e,f show the θ and ϕ distributions of galaxies in the substructures S3. If we look at the observed distribution of galaxies in the polar angle, humps (2.5°, 22.5°, 37.5°, 47.5°, 57.5°, 67.5°) and dips (7.5°, 12.5°, 42.5°, 77.5°, 77.5°) at both smaller and larger angles are seen. In the statistical tests, these humps and dips cancel each other to show isotropy in the θ distribution. In the ϕ distribution, the statistical parameters P($> \chi^2$), P($> \Delta_1$) and $\Delta_{11}/\sigma(\Delta_{11})$ show isotropy (Table 1) whereas the auto correlation coefficient (C/C(σ)) shows a small deviation (1.1σ) from isotropy. Similar to Fig. 4e, a large number of humps and dips are seen in the ϕ distribution (Fig. 4f). The successive deviation in the alignments might be a clue regarding the substructure formation in the supercluster. So, the distribution of such a local effect should be studied in the future.

The fourth substructure S4[183+0050+0080] has 67 galaxies with mean redshift 0.080, which is larger than that of substructures S1, S2 and S3. In other words, this substructure is leading in terms of mean radial velocity. If we look at the distributions (θ and ϕ, Fig. 4g,h), a poor agreement between the observed and expected values is seen. A large number of humps (at 2.5°, 12.5°, 32.5°, 47.5°, 57.5° in θ; at −85°, −45°, −35°, −15°, 15°, 25°, 45°, 65° in ϕ) and dips (at 7.5°, 17.5°, 22.5°, 42.5°, 77.5° in θ; at −75°, −65°, −15°, 5°, 15°, 55°, 75°, 85° in ϕ) can be seen. All these humps and dips are at $>1\sigma$ level. In contrast to these successive and alternative humps and dips, in the statistical tests, all four statistical parameters suggest strong isotropy. There-

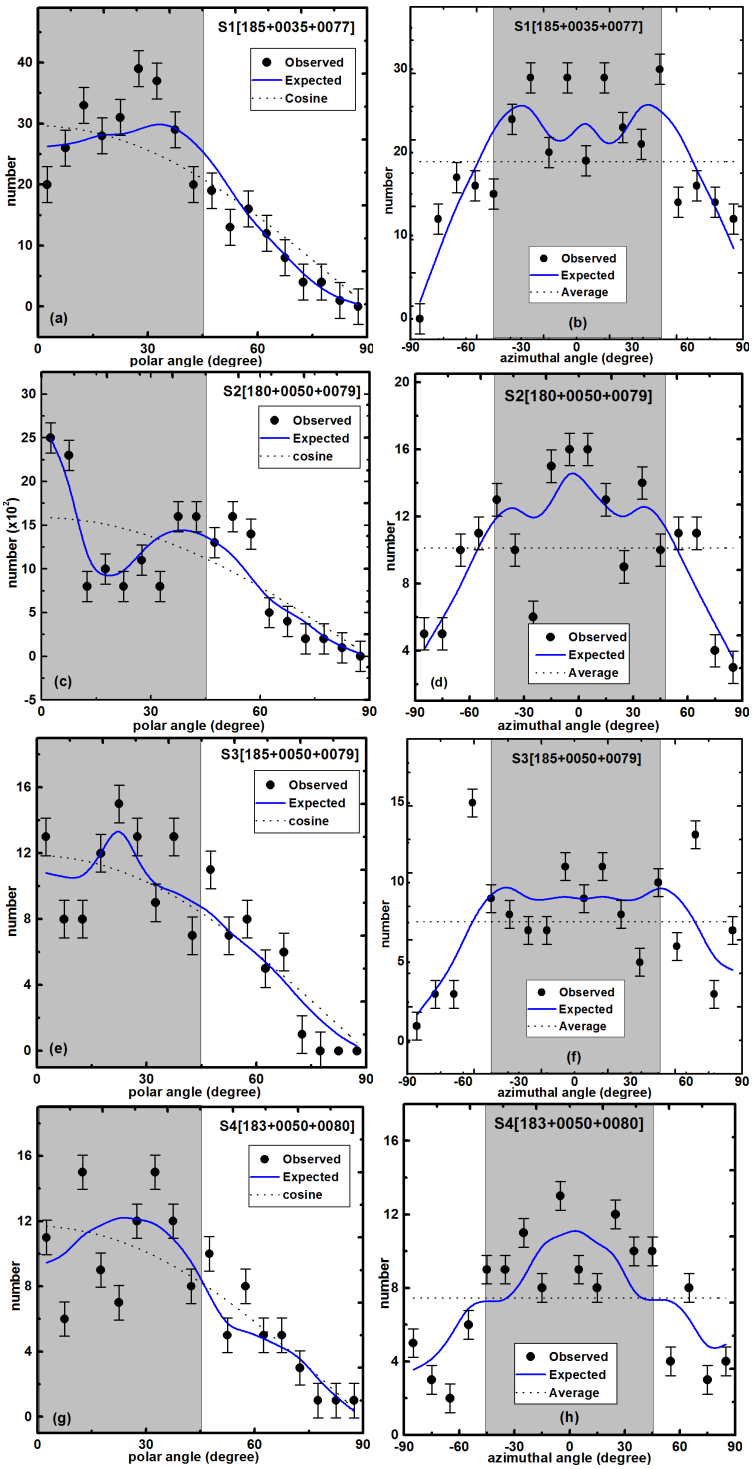

Fig. 4. Polar (a,c,e,g) and azimuthal angle (b,d,f,h) distributions of galaxies in the substructures of supercluster S[184+003+0077]. The solid curves represent the expected distributions. The dashed curves show the cosines (a,c,e.g) and average (b,d,f,h) distributions. The statistical $\pm 1\sigma$ error bars are shown. The names of the substructures are given.

fore, the substructure S4 shows 'vanishing angular momentum' as suggested by Godlowski et al. (2010).

Melkonian & Nikogosian (1998) studied a substructure of the core of the Perseus Supercluster of galaxies. They noticed hierarchical substructures in which a radial segregation of galaxies is found. However, the position angle distribution of galaxies is found to be uniform. Godlowski et al. (1998) studied the rich cluster of galaxies Abell 754 and found evidence for non-random alignment of the galaxies and confirmed the presence of subclustering.

Baier et al. (2003) studied the galaxy cluster Abell 14 and confirmed the presence of subclustering. They noticed a preferred alignment of the angular momentum vectors of galaxies in the cluster Abell 14. Norena et al. (2018) proposed an idea that substructures could be formed due to the tidal stream produced in galactic mergers. Panko et al. (2018) investigated the 2D distribution of galaxies in 254 rich open galaxy clusters. They noticed that about 25% of clusters showed four kinds of regular substructures namely crossing and divaricating filaments (or X and Y-type peculiarities) and curved strips with short dense chains. Malla et al. (2020) studied the preferred alignments of galaxies in the SDSS supercluster S[202-001+0084]. They noticed a random orientation of the angular momentum of galaxies in this supercluster. We also noticed a similar result in the supercluster S[184+003+0077].

To sum up, we noticed a random orientation of the angular momentum vectors and their projections in the supercluster S[184+003+0077], as well as in all four substructures S1[185+0035+0077], S2[180+0050+0079], S3[185+0050+0079] and S4[183+0050+0080] with a signature of local groupings. We intend to study the alignment of galaxies in these small groups in the substructure to reveal the reason behind it.

5 Conclusion

We have studied the distribution of the nearest neighbor galaxies to find substructures in the supercluster S[184+003+0077] region. The spatial orientation of 1 365 galaxies in the supercluster S[184+003+0077] having a redshift of 0.077 and its substructures are studied. We summarize our results as follows:

1. Four substructures are found in the supercluster S[184+003+0077]. These are S1[185+0035+0077], S2[180+0050+0079], S3[185+0050+0079] and S4[183+0050+0080] with a mean redshift of 0.077, 0.079, 0.079 and 0.080, respectively. An empirical relation between the mean redshift ($< z >$) and the number of galaxies (N) in the substructures is found.
2. The distribution of the angular momentum vectors of galaxies in the supercluster S[184+003+0077] showed isotropy, suggesting no preferred alignments. In the substructures, despite having alternate and successive deviations from the expected distributions, the overall effect is found to be that of a vanishing angular momentum. Thus, no preferred alignments of the angular momentum vectors of galaxies are found in the supercluster and its all four substructures, supporting the hierarchy model (Peebles, 1969).
3. The projections of the angular momentum vectors of galaxies in the supercluster S[184+003+0077] is found to be random. In the substructures, these projections are found to be alternately deviated from the expected distribution. However, isotropy is found to be maintained.

4. The substructures showed higher values of the mean redshift than that of the supercluster S[184+003+0077]. This corresponds to the fact that the subclusters are moving with higher radial velocities than that of the supercluster. Thus, the gravitational shearing effect can not be ruled out in the large scale structure formation (Li, 1998)

Acknowledgement

We are thankful to anonymous reviewer for critical and constructive comments and suggestions. One of the authors (JRM) acknowledges Nepal Academy of Science & Technology, Central Department of Physics, Amrit Campus, Tribhuvan University, Nepal for various kinds of support during Ph.D. work. We are thankful to Dr. Shiv Narayan Yadav, Mr. Ek Narayan Poudel, Mr. Mohan Gaire and Mr. Balendra Bhatt for their help during data compilation. We have used SDSS database (https://classic.sdss.org/dr7/), SIMBAD (http://simbad.u-strasbg.fr/simbad/) for providing database and software ALADIN 2.5 (https://aladin.u-strasbg.fr/).

References

Aryal B., Paudel S., Saurer, W., 2007, *MNRAS* 379, 1011
Aryal B., Saurer W., 2000, *A&A* 364, L97
Baier F. W., Godlowski W., MacGillivray H. T., 2003, *A&A* 403, 847
Einasto J., Hütsi G., Einasto M., Saar E., Tucker D. L. et al. 2003, *A&A* 405, 425
Einasto M., Liivamägi L. J., Tago E., Saar E., Tempel E. et al., 2011, *A&A* 532, 20
Einasto M., Lietzen H., Tempel E. Gramann M. Liivamägi L. J. et al., 2014, *A&A*, 562, 14
Einasto M., Lietzen H., Gramann M., Tempel E., Saar E. et al., 2016, *A&A* 595, 12
Flin P., Godlowski W., 1986, *MNRAS* 222, 525
Gamow G., 1952, *Phys. Rev.* 86(2), 251
Godlowski W., 2012, *ApJ* 747, 1, 7
Godlowski W., 1994, *MNRAS* 271, 19
Godlowski W., Baier F. W., MacGillivray H. T., 1998, *A&A* 339, 709
Godlowski, W., Piwowarska, P., Panko, E., Flin, P., 2010, *ApJ* 723, 2, 985
Holmberg, E., 1946, *Medd. Lund. Astron. Obs.*, Ser. VI, No. 117
Li, L. X. 1998, *General Relativity and Gravitation* 30, 497
Liivamägi L. J., Tempel E., Saar E., 2012, *A&A* 539, 14
Malla, J. R., Saurer, W., Aryal, B., 2020, *Galactic Dynamics in the Era of Large Surveys*, Proceedings of the International Astronomical Union, Vol. 353, 259.
Melkonian A. A., Nikogosian E. G., *Astrophysics* 41, 1, 41
Norena D. A., Muñoz-Cuartas J. C., Quiroga L. F., Libeskind N., 2019, *Revista Mexicana de Astronomía y Astrofísica* 55, 273
Ozernoy L. M., 1978, in Longair M. S., Einasto J., eds, Proc. IAU Symp. 79, The Large Scale Structure of the Universe. Reidel, Dordrecht, p.427
Panko E. A., Andrievsky S. M., Yemelianov S. I., Stepaniuk A. M., 2018, *Astron. Reports* 62(12), 911
Peebles P. J. E., 1969, *ApJ* 155, 393
Shandarin S. F., 1974, *Astr. Zh* 51, 667 (in Russian), Soviet Astron 18, 392 (in English)
Von Weizsäcker C., 1951, *ApJ* 114, 165

Appendix A

Galaxy Counting Code (MATLAB 6.1)
ra = importdata('ra.m');
dec = importdata('dec.m');

```
sc = [ra,dec];
n = numel(ra) repeat = 'y';
while repeat =='y' radius = input('Enter the radius of circle in degree: ') for
i=1 : n count=0;
for j=1 : n r = (ra(i) - ra(j))^2 + (dec(i) - dec(j))^2;
if r <= radius*radius count=count+1;
end
end
neighgal(i)=count;
end str = input('enter a −le name to store near galaxy numbers: ','s') −d=fopen(str,'wt');
fprintf(−d,'fclose(−d);
repeat=input('enter c if you wish to continue for another size or e to exit:
'end')
```

Analysing the Time Period of the Vela pulsar

Shreyan Goswami[1], Hershini Gadaria[1],
Sreejita Das[1], Midhun Goutham[1], Kamlesh N. Pathak[1]
Sardar Vallabhbhai National Institute of Technology,
Surat, India
goswamishreyan@gmail.com, i19ph041@phy.svnit.ac.in,
i19ph017@phy.svnit.ac.in, i19ph050@phy.svnit.ac.in, knp@phy.svnit.ac.in
(Submitted on 28.02.2022. Accepted on 22.05.2022)

Abstract. In this project, we have implemented our basic understanding of Pulsar Astronomy to calculate the time period of the Vela pulsar. Our choice of pulsar rests on the fact that it is the brightest object in the high energy gamma ray sky. The simplistic data set consisting of only voltage signals makes our preliminary attempt as closely accurate as possible. The observations had been made at 326.5 MHz through a cylindrically paraboloid telescope at Ooty. A higher frequency creates a much lower delay in the arrival time of pulses and makes our calculations even more accurate. Being an already widely studied celestial body, it gives us the opportunity to compare our findings and make necessary modifications.

Introduction

Pulsars are rapidly rotating highly magnetised neutron stars. They emit two steady, narrow beams of electromagnetic radiation in opposite directions that sweep the sky like a lighthouse. Pulsars are of extreme importance to astronomers as they can help locate planets or other celestial bodies orbiting around it, measure the distance to galaxies, construct models of free electron distribution and detect gravitational waves. Calculating several parameters of known pulsars like their distance or time period can allow us to perform further complex calculations and estimations, helping us gain a much deeper understanding of the universe. We have been provided with a raw voltage signal from the observation of the Vela Pulsar ($PSRB0833-45$) by the two sub-apertures (north and south) of the Ooty Radio Telescope.(Arumugasamy, P., 2021) It is a cylindrical paraboloid telescope based on a north-south slope of 11.2 degrees in Ooty. The reflecting surface is 530m long and 30m wide and is operated at 326.5 MHz. The large reflecting surface makes the telescope highly sensitive. The observations, as recorded in the data set, have been made at 326.5 MHz with a bandwidth of 16.5 MHz. A data set with one second's worth of data was used with each row of data being separated by 30 nano seconds 33.3(3) MHz. The main difference in the analysis being, we have used the DM (Dispersion Measure) that has already been found to make sure our results have increased accuracy. The analysis was also compared to The ATNF Pulsar Catalogue (Manchester, R. N.et all., August 2005) for understanding how close we were to the real value.

In section 1 we have explored the statistical characteristics of the brown Vela pulsar to make sure there are no discrepancies in data. Voltage and power signals are plotted to understand what the distribution of the data is.

Section 2 discusses properties of the signal and dynamic spectrum. This section discusses the Radio Frequency Interference (RFI) and how one would eliminate it. The frequency delay results from the same.

In section 3 we find the distance using the correct values of DM to show that the same shall be applied to find a more accurate time period that allows us to eliminate the time delays by using the DM and to get a dedispersed time series of the pulsar. In further sections, we find the average time period and plot the average profile of the pulsar.

1 Statistical characteristics of the signal

1.1 Voltage signal characteristics

We began our analysis by performing statistical evaluation of the raw voltage signals to verify some of its expected properties. We expect the signals to have a Gaussian distribution. To do this, we randomly and uniformly selected 100,000 voltage samples from both the north and the south arrays and plotted the histogram. As expected, the voltage signals demonstrate Gaussian distribution.

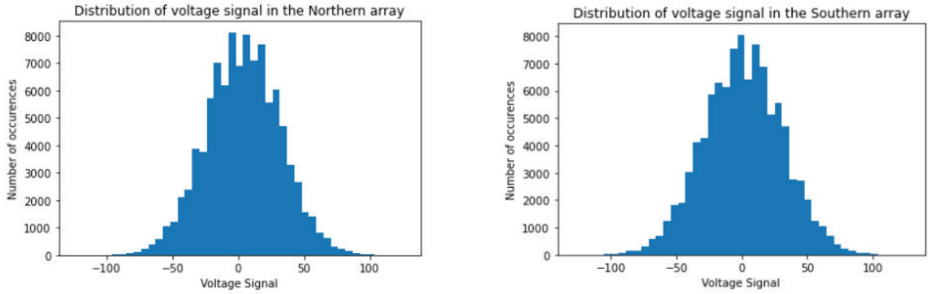

Fig. 1. (a) Histogram for northern array; (b) Histogram for southern array
Voltage signal distribution of 100,000 randomly selected samples

1.2 Power signal characteristics

We further studied the distribution that the power signals follow. The power or intensity signal is merely the square of the voltage signal. The power signals are expected to follow an exponential distribution. We used the same data samples that we used to look at voltage characteristics previously. Histograms for both the northern and southern arrays were plotted. As expected, the power signals demonstrate an exponential distribution.

2 Properties of the signal in the Time-Frequency domain

2.1 Voltage power spectrum

The power spectrum of a signal describes the power present in the signal as a function of frequency. Any physical signal can be decomposed into a spectrum

of frequencies over a range. We used a very efficient algorithm known as the Fast Fourier Transform (FFT) to plot the power distribution as a function of frequency.

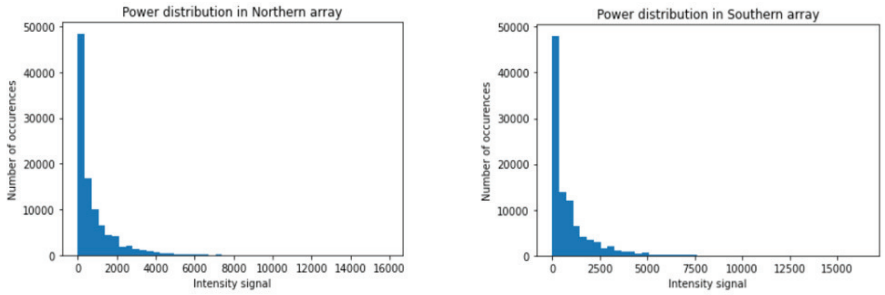

Fig. 2. (a) Histogram for northern array; (b) Histogram for southern array
Power signal distribution of 100,000 randomly selected samples

To compute the FFT, 256 frequency channels were used since power of 2 increases the speed of FFT (in this case, 16^2). The average power spectrum of the voltage signal was plotted by averaging the power spectrum obtained from all 512-point FFTs. The voltage power spectrum for both the northern and southern arrays are given in figure 3. Each corresponds to an interval of 512/33 microseconds. The sharp peaks in the spectra might indicate the presence of local RFI. RFI is a disturbance caused by an external source like cellular networks, lightning, solar flares, etc that affects the electrical circuit used to originally measure the voltage signals from the pulsar. As observed, the DC channel power is much larger in the northern array than in the southern. The plot smoothly tapers off to 0 at both edges, indicating that the aliasing is minimal.

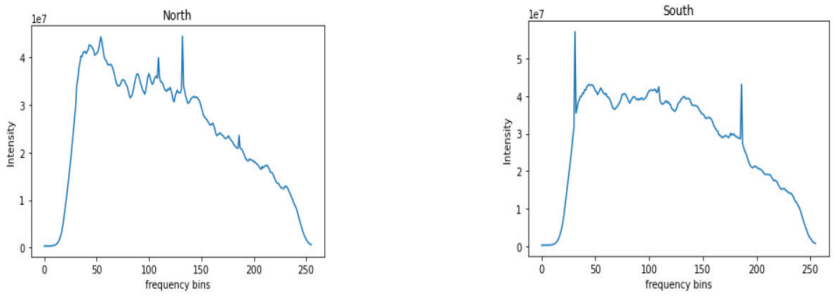

Fig. 3. (a) Voltage power spectrum for northern array; (b) Voltage power spectrum for southern array
Average voltage power spectrum for both the arrays. The frequency axis ranges from 0 to 256 MHz

2.2 Dynamic spectrum

The dynamic Spectrum is a color-coded graph that shows the relationship between frequency (MHz) and time (ms). It enables us to detect pulsar signal indicators. Incoherent addition was used to combine the power from the two halves of the array to increase the Signal to Noise Ratio (SNR). Incoherent addition helped in removing RFI to a large extent. The dynamic spectrum is shown below. The x-axis represents time measured in ms and the y axis represents frequency in MHz. The colour bar on the right indicates the intensity of the power signal for a particular time and frequency data point. The diagonal and uniformly spaced features shown in the graph above leads us to conclude that the source has to be a pulsar.

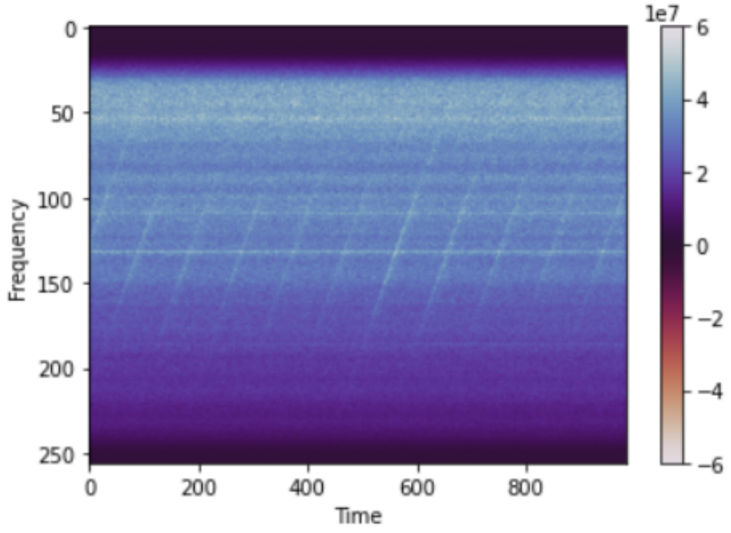

Fig. 4. The dynamic spectrum of the signal. Frequency (in MHz) is plotted on the y-axis, and decreases upwards. Time is plotted on the x-axis for a duration of 1000 ms.

Upon carefully observing each pulse, the signal appears first at higher frequencies, and gradually appears later at lower frequencies. Thus, there is a frequency delay in the observed data which is a characteristic sign of a signal dispersed in the interstellar medium.Since our analysis is concerned with magnitudes, negative intensities at either ends of the colour bar do not pose any discrepancy.

2.3 Dispersion measure and the frequency delay

The dispersion measure (DM) is a parameter that shows up in observations as the broadening of an otherwise sharp pulse. In statistics, it refers to how far a distribution may be stretched or squeezed. The DM is measured in pc/cm^3 and is calculated as:

$$t \approx t_\infty + 4.149 \times 10^3 \times DM \times \nu^{-2} \tag{1}$$

where t is the pulse arrival time in seconds and t_∞ is the pulse arrival time in seconds at infinite frequency. The DM is equal to 67.62 pc/cm^3. (Caraveo, P. A. et al. 2001)

The electrostatic interaction between radio waves and charged particles in the Interstellar Medium creates a delay in the propagation of light, with the delay being a function of radio frequency and the masses of the charged particles or the dispersion measure. The lower the frequency, the greater the delay. The delay is given by:

$$\tau(s) = 4.149 \times 10^3 \times DM \times (\nu_1^{-2} - \nu_2^{-2}) \tag{2}$$

3 Distance to the pulsar

The distance to the pulsar (S) is given by:

$$S = \frac{DM}{n_e}, \tag{3}$$

where n_e is the mean electron density between the pulsar and earth and is equal to 0.23 $percm^3$. (Caraveo, P. A. et al., 2001), (Toscano, M. et al., 1999) Hence, S = 294 pc.

4 Dedispersed time series

We eliminated the frequency-dependent time delays using the DM. To obtain the de-dispersed signal intensity, we changed the time-domain position of all lower frequency channels to align them with the pulse arrival time at the highest channel using Equation (1), and then added the same for all the channels. The obtained dedispersed time series is given below. The peaks in the above graph are much more significant and easier to recognize among the background noise. This is due to the dedispersion procedure increasing the SNR.

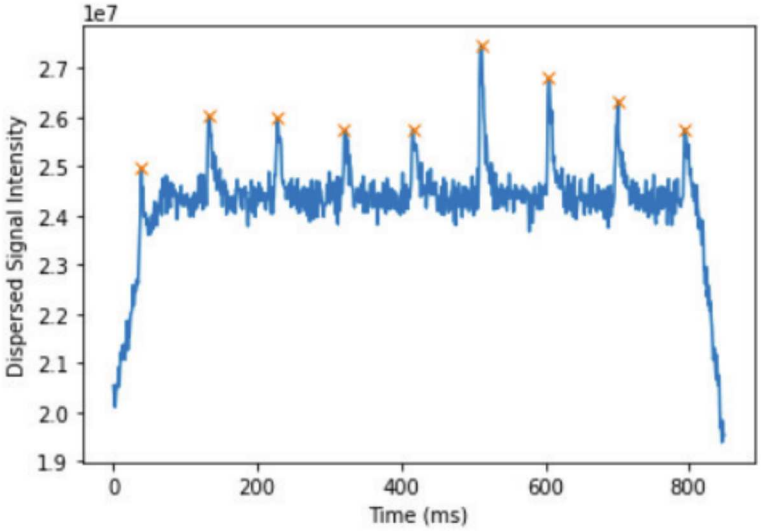

Fig. 5. The dedispersed time series.

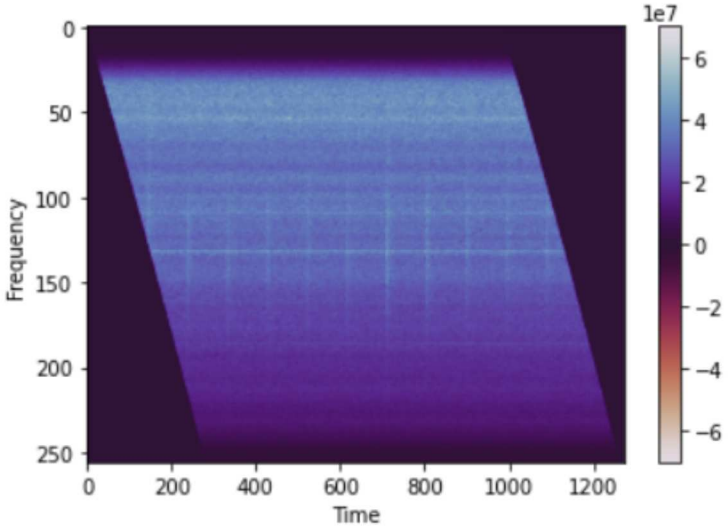

Fig. 6. The dynamic spectrum after accounting for the time delay

5 Time period of the pulsar

We obtained a series of significant periodic single pulses in the previous section. This enabled us to further calculate the time period of the pulsar.The arrival time of the individual pulse should fit a period-solution, and hence, we used

the technique of curve fitting, to estimate the arrival times. The best fit curve is a linear curve as given in the figure below.

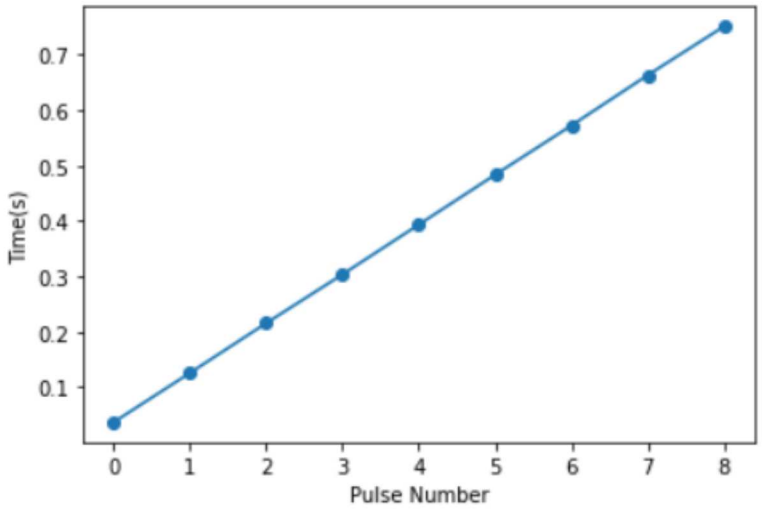

Fig. 7. Fitting a linear curve to estimate the arrival times

The arrival time of each pulse has been tabulated below.

Pulse number	Arrival time (ms)	Uncertainty(ms)
1	88.96388	0.33612
2	178.8742	0.610303
3	266.8916	1.28255
4	356.8019	0.610303
5	446.7122	0.610303
6	535.6761	0.33612
7	624.6761	0.3

Table 1. Pulse arrival times.

Based on the arrival times as shown in the table above, the time period of the pulsar is 89.28537 ms.

5.1 Error analysis

The calculated mean time period of the Vela pulsar is 89.28537 ms. Comparing this mean to the expected time period as obtained from the ATNF Pulsar

Catalogue (Manchester, R. N. et al., 1993) results in a 0.04772 % error. The calculated standard deviation of the time period is 0.70287.

Finally, based on the time period, we folded the entire time series with the pulsar period to obtain an average profile for the pulsar.

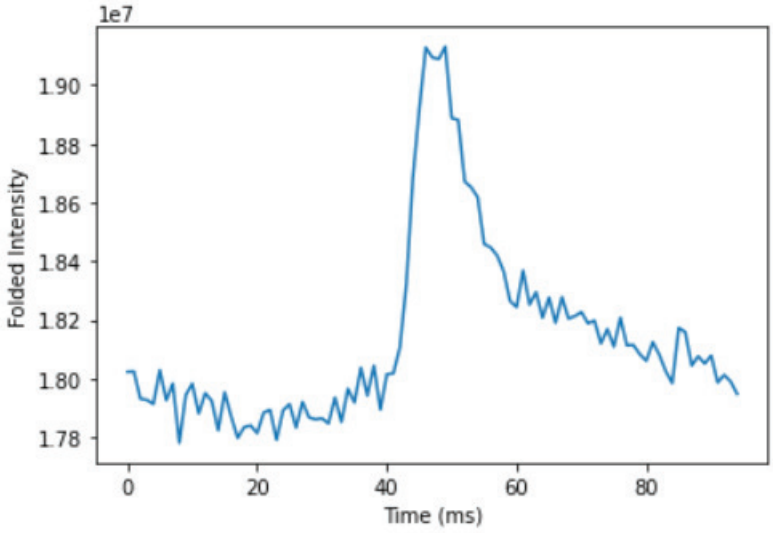

Fig. 8. The average profile of the pulsar.

6 Conclusion

After implementing various techniques, we managed to calculate important parameters related to the pulsar.We also examined the statistical properties of the raw voltage signal.

- We estimated a distance of 294 pc to the pulsar from a dispersion measure of 67.62 pc/cc. The distance calculated is in agreement with the value measured using the method of parallax, considering the error margin. (Caraveo, P. A. et al., 2001)
- The time period of the pulsar turned out to be 89.28537 ms. brownThe calculated time period is in agreement with the currently accepted value obtained from the ATNF Pulsar Catalogue. (Manchester, R. N. et al., 1993) This is more accurate as we used the exact value of the density measure. (Özsükan, G.et al., 2014)

An important thing to note is that all the quantitative figures are estimates with some amount of uncertainty. This can be due to uncertainties in other parameters such as the dispersion measure, low exposure time, small dataset etc. Longer observation time would significantly reduce uncertainties

in the data. Since the source is a compact object, the visibility should remain constant as a function of time. Hence, the Fourier Transform of the brightness distribution should not change with a change in baseline. Over the course of the project, we gained invaluable insight into the analysis of pulsars and how to decipher information from mere observations.

The code used for analysis is available:
https://colab.research.google.com/drive/1xKyDeazvLapjxktVDaM9-3Qv1Evv64S3?usp=sharing

Acknowledgement:
The authors would like to express their gratitude to Dr. Avinash Deshpande, who provided us the raw signal data, and Mr. Devansh Shukla, who helped in the course of the project. HG would like to thank Department of Science and Technology of India for the INSPIRE Scholarship for Higher Education (SHE), (DST/INSPIRE/02/2019/011921).

References

Caraveo, P. A., De Luca, A., Mignani, R. P., Bignami, G. F., 2001. The distance to the Vela pulsar gauged with hubble space telescope parallax observations. *The Astrophysical Journal, 561(2), 930.*

Özsükan, G., Ekşi, K. Y., Hambaryan, V., Neuhäuser, R., Hohle, M. M., Ginski, C., Werner, K., 2014. The Vela pulsar with an active fallback disk. *The Astrophysical Journal, 796(1), 46.*

Toscano, M., Britton, M. C., Manchester, R. N., Bailes, M., Sandhu, J. S., Kulkarni, S. R., Anderson, S. B., 1999. Parallax of PSR J1744–1134 and the local interstellar medium. *The Astrophysical Journal Letters, 523(2), L171.*

Arumugasamy, P., 2021. Detecting a Pulsar in Ooty Radio Telescope Voltage Data. IUCAA-ACE/radio/Exp004:
http://hdl.handle.net/11007/4565

Manchester, R. N.; Hobbs, G. B.; Teoh, A.; Hobbs, M., August 2005. The Australia Telescope National Facility Pulsar Catalogue. *The Astronomical Journal, 129(4), 1993*